Image Reconstruction of Electrical Impedance Tomography Based on Optical Image-Guided Group Sparsity

Image Reconstruction of Electrical Impedance Tomography Based on Optical Image-Guided Group Sparsity

Zhe Liu, *Student Member, IEEE*, Yunjie Yang, *Member, IEEE*

Abstract—**The low spatial resolution of Electrical Impedance Tomography (EIT) makes it challenging to conduct quantitative analysis of the electrical properties of imaging targets in biomedical applications. We in this paper propose to integrate optical imaging into EIT to improve EIT image quality and report a dual-modal image reconstruction algorithm based on optical image-guided group sparsity (IGGS). IGGS receives an RGB microscopic image and EIT measurements as inputs, extracts the structural features of conductivity distribution from optical images and fuses the information from the two imaging modalities to generate a high-quality conductivity image. The superior performance of IGGS is verified by numerical simulation and real-world experiments. Compared with selected single-modal EIT image reconstruction algorithms, i.e. the classical Tikhonov regularization and the state-of-the-art Structure-Aware Sparse Bayesian Learning and Enhanced Adaptive Group Sparsity with Total Variation, the proposed method presents superiorities in terms of shape preservation, background noise suppression, and differentiation of conductivity contrasts.**

Index Terms—**Dual-modal imaging, miniature impedance-optical sensor, electrical impedance tomography, information fusion, image reconstruction**

I. Introduction

Electrical Impedance Tomography (EIT) is a tomographic imaging modality, which estimates the conductivity distribution within a 2D or 3D bounded domain from a sequence of boundary voltage measurements [1-3]. EIT offers non-radiative, non-intrusive and high-temporal-resolution imaging capabilities and is investigated in many research domains, such as flow velocity field measurement [4], chemical engineering [5], multiphase flow monitoring [6, 7], and non-destructive cell culture imaging in tissue engineering [8-10]. However, its low image quality as a longstanding challenge has become a critical issue that prevents its wider adoption in different fields.

The challenge of improving EIT image quality involves the structure preservation of imaging targets, differentiation of conductivity contrasts and suppression of artefacts and noise. In recent years, research to address the challenge for 'single-modal' EIT is mainly in concerned with image reconstruction algorithms. Many algorithms leverage regularization to deal with the severe ill-posedness of the EIT inverse problem. This type of algorithms encodes certain prior information through the penalty term to stabilize the solution. These methods include Total Variation (TV) regularization [11, 12], Fidelity-Embedded regularization [13], sparse regularization [14-16], Adaptive Group Sparsity (AGS) regularization [17, 18], and Sparse Bayesian Learning (SBL) [19], etc. Although these

methods have brought a vast improvement in image quality, they can hardly precisely recover the shape and conductivity of the imaging targets simultaneously. Many algorithms are powerless when the geometry of the imaging target includes straight lines and angles. Shape-based image reconstruction methods were proposed to address better shape recovery. Such methods focus on the recovery of the shape of imaging targets regardless of the conductivity values and it can directly introduce the prior information of the shape into the image reconstruction procedure [20-22]. These methods present superior results to the regularization-based methods in terms of shape preservation. However, the image quality improvement for EIT is still limited because the conductivity and the shape of the imaging target cannot be simultaneously estimated accurately based only on EIT measurements. Therefore, dual-modal or multi-modal EIT imaging is proposed to overcome such issue and it utilizes other imaging modalities as supplements to EIT, which could provide additional information to improve the EIT image quality. Some work on dual-modal or multi-modal based EIT image reconstruction has been reported. Li et al. developed a CT image guided method for EIT inversion, and the proposed algorithm showed the advantage of improved ability of shape preservation [23]. Another representative work is related to EIT and ultrasound tomography (UT) joint imaging which is based on the complementary sensitive areas of these two modalities [24, 25]. Reconstructed images based on EIT and UT also presented a better image quality compared with those based on single-modal EIT.

However, simultaneous, accurate recovery of conductivity and shape remains a significant challenge for EIT. In this paper,

Z. Liu and Y. Yang are with the Intelligent Sensing, Analysis and Control Group, Institute for Digital Communications, School of Engineering, The University of Edinburgh, Edinburgh, UK, EH9 3JL (Corresponding author: Yunjie Yang, e-mail: y.yang@ed.ac.uk).
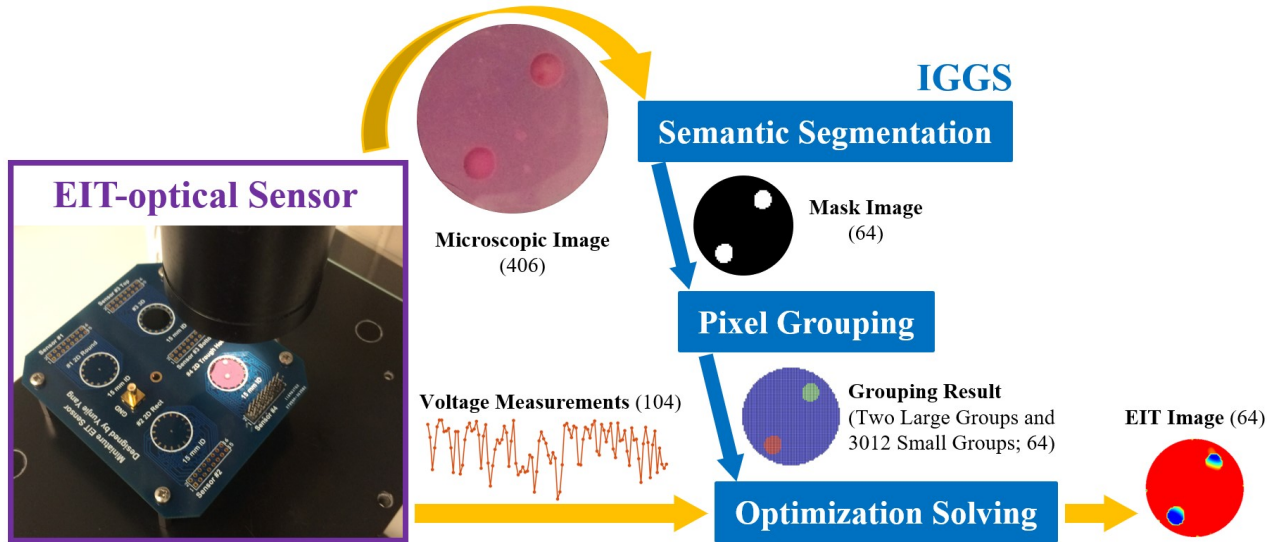
Fig. 1. Schematic of the dual-modal imaging framework. 406 and 64 represent the side lengths of the circumscribed square regions for circular images. 104 is the dimension of voltage measurement vector.

we propose an EIT-optical dual-modal imaging approach to address the above-mentioned challenges. We propose Image-Guided Group Sparsity (IGGS) for information fusion and high-quality conductivity reconstruction by leveraging the EIT measurements and microscopic images from a miniature impedance-optical dual-modal sensor as input. IGGS provides a new way to incorporate the structural information contained in the microscopic image into EIT image reconstruction by using the group sparsity regularization, which has been comprehensively investigated in single-modal EIT image reconstruction [17, 18]. IGGS adopts pixel grouping to link group sparsity with the structural information extracted from microscopic image segmentation. The finally established optimization problem is solved by the Accelerated Alternating Direction Method of Multipliers (A-ADMM) [26]. The results of the proposed method and the given single-modal based algorithms, i.e. Tikhonov regularization (TReg) [27], Structure-Aware Sparse Bayesian Learning (SA-SBL) [19] and Enhanced Adaptive Group Sparsity with Total Variation (EAGS-TV) [18], are thoroughly compared by simulation and real-world experiments.

The paper is organized as follows. Section II briefly describes the principle of the EIT inverse problem. Section III states the proposed imaging framework and IGGS. Section IV presents simulation and experimental results and compares algorithm performance. Finally, Section V concludes the work and discusses future work.

II. PRINCIPLE OF EIT IMAGE RECONSTRUCTION

In EIT, the relationship between the conductivity distribution and the induced boundary voltage can be expressed by the following non-linear equation:

$$V = F(\sigma) + E \tag{1}$$

where $F: \mathbb{R}^n \to \mathbb{R}^m$ is the non-linear forward mapping of EIT. $V \in \mathbb{R}^m$ represents the measured boundary voltage, $\sigma \in \mathbb{R}^n$

denotes the conductivity distribution, and $E \in \mathbb{R}^m$ stands for the measurement noise. In this study, we adopt the time-difference imaging method. The linearized forward model with respect to the conductivity change $\Delta\sigma \in \mathbb{R}^n$ and the induced boundary voltage change $\Delta V \in \mathbb{R}^m$ between the reference time point and the observation time point exists [28]:

$$\Delta V = J\Delta\sigma + e \tag{2}$$

where $J \in \mathbb{R}^{m \times n}$ is the Jacobian matrix; $e \in \mathbb{R}^m$ is the measurement error removing the common components in the two measurements. As time-difference imaging can, to a certain extent, eliminate the common measurement errors, this approach has better noise resistance ability and resistance to the imperfection of miniature sensors compared to absolute imaging. Therefore, it is more suitable for biomedical imaging applications with miniature EIT sensors, which is more challenging as the signals are weaker and the measurements are more sensitive to the imperfection of the sensor due to fabrication limitations.

Under the time-difference imaging framework, the general approach to estimate $\Delta\sigma$ through ΔV can be formulated as the following optimization problem:

$$\begin{cases} \min_{\sigma} & Q(\Delta\sigma) \\ \text{s.t.} & J\Delta\sigma = \Delta V \end{cases} \tag{3}$$

where Q is the regularization function, which is determined by the prior information of the conductivity change distribution.

III. METHOD

The EIT-optical dual-modal imaging approach (see Fig. 1) is based on image-guided group sparsity (IGGS). The impedance-optical sensor will simultaneously record and output a frame of voltage change measurements and an RGB microscopic image. Then, IGGS will fuse the two types of information from different modalities and generate a high-quality EIT image. The details are described in the following subsections.

A. EIT-optical Dual-modal Sensor

The manufactured dual-modal sensor is shown in Fig. 1. It comprises a miniature 16-electrode EIT sensor and a digital microscope (Digital USB Microscope 1.3M, RS Components Ltd). The EIT sensor is placed under the microscope and the two sensors share the same sensing region. We select two different EIT sensors to investigate our method. They are labelled as EIT sensor A (see Fig. 2 (a)) and EIT sensor B (see Fig. 2 (b)). The two EIT sensors are both manufactured on the Printed Circuit Board (PCB).

The sensing area of EIT sensor A is bounded by the PCB board (bottom of the sensing area) and a transparent glass tube (see Fig. 2 (a)). The height and the inner diameter of the glass tube are 6 mm and 15 mm, respectively. Sixteen gilded square microelectrodes are manufactured on the surface of the PCB and uniformly distributed at the bottom of the sensing area.

The imaging targets in EIT sensor B are placed on the transparent glass substrate at the bottom of the sensing domain (see Fig. 2 (b)). The sidewall of the sensing region is surrounded by the PCB and microelectrodes. The height of microelectrodes is the same as the thickness of the PCB, i.e. 1.6 mm. The diameter of the sensing area is 15 mm. Sixteen gilded microelectrodes are manufactured using the half-hole process and uniformly distributed at the periphery of the sensing area.

B. Image-Guided Group Sparsity

IGGS consists of three steps (see Fig. 1). In the first step (semantic segmentation), the input RGB microscopic image is converted into its binary version. The height and width of the converted binary image (named mask image) is the same as those of the EIT image. In the second step (pixel grouping), the pixels of the EIT image are partitioned into different groups based on the mask image. In the last step (optimization solving), the grouping result first navigates the construction of the group sparsity regularization term. Afterwards, the final optimization problem will be established and solved by the Accelerated Alternating Direction Method of Multipliers (A-ADMM) [26]. Each step of IGGS is described as follows.

1) Semantic Segmentation: The purpose of semantic segmentation is to generate the mask image of the input microscopic image. The algorithm in this step is replaceable because it highly depends on the configuration of the dual-modal sensor and the application of the imaging system. As stated in Section III-A, there are two EIT sensors to conduct experiments in this work and they possess disparate structures, which leads to distinct types of microscopic images. For example, electrodes usually appear in the microscopic image generated by EIT sensor A based dual-modal sensor, while this situation does not happen in the microscopic image generated by EIT sensor B based dual-modal sensor. Thus, the electrodes should be eliminated in the semantic segmentation for images based on EIT sensor A based dual-modal sensor. Therefore, different sets of semantic segmentation algorithms should be applied to these sensors, and each set of algorithms include multiple image operations.

The first set of segmentation algorithms is developed for EIT sensor A based dual-modal sensor. In operation 1 (OPA1), an RGB difference image is generated by subtracting the calibration image from the carrot image. The calibration image can be collected before real-time imaging and there are no
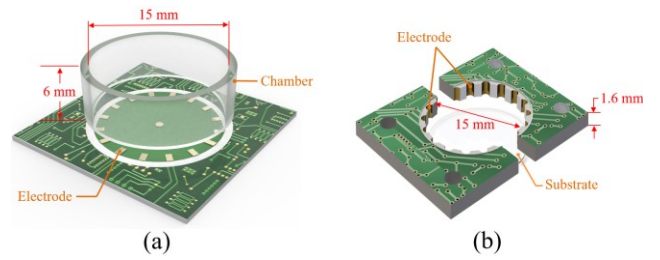

Fig. 2. Structure of (a) EIT sensor A and (b) EIT sensor B.

imaging targets in the calibration image. In operation 2 (OPA2), the RGB difference image is firstly converted into its grayscale version. Then, Otsu's method based segmentation algorithm is applied to this grayscale image to transform it into a binary image. Otsu's method, as a histogram technique in image segmentation fields, finds the global value threshold in a grayscale image [29]. According to the calculated grayscale value threshold, pixels with the value above the threshold will be transformed to white (digit 1) and other pixels will be transformed to black (digit 0). The formula of Otsu's method for threshold searching is expressed by:

$$t^* = \arg\max_{1 \le t \le L} \frac{[(\sum_{\ell=1}^{L} \ell p_\ell)(\sum_{\ell=1}^{t} p_\ell) - \sum_{\ell=1}^{t} \ell p_\ell]^2}{(\sum_{\ell=1}^{t} p_\ell)[1 - \sum_{\ell=1}^{t} p_\ell]} \quad (4)$$

where, t^* is the optimal threshold of a grayscale image. L is the total gray levels of this image and $p_\ell = \frac{q_\ell}{n}$; q_ℓ is the number of pixels at ℓ^{th} gray level and n is the total number of pixels of the image.

In operation 3 (OPA3), open operation and dilation operation are applied successively to the binary image generated by OPA2 to refine the object's boundary. Then, the result is down-sampled to the EIT image size. Operation 4 (OPA4) is to eliminate small connected white regions to acquire the ultimate mask image. The threshold pixel number for the small connected white region is based on specific applications. This parameter is set as 50 throughout the paper. The two morphological operations in OPA3 are defined as [30]:

$$I \circ S = \cup \{(S)_z | (S)_z \subseteq I\} \quad (5)$$

$$I \oplus S = \left\{ z \middle| (\hat{S})_z \cap I \ne \emptyset \right\} \quad (6)$$

where, $I \circ S$ means image I is opened by the structuring element S and $I \oplus S$ means I is dilated by S. $(S)_z$ and $\hat{S}$ are defined as:

$$(S)_z = \{k | k = \psi + z, \psi \in S\} \quad (7)$$

$$\hat{S} = \{\vartheta | \vartheta = -\psi, \psi \in S\} \quad (8)$$

where $z = (z_1, z_2)$ is a fixed point in the image. Fig. 3 provides an example of the first semantic segmentation procedure.

The second set of segmentation algorithms is applied to EIT sensor B based dual-modal sensor and it also includes four operations. Operation 1 (OPB1) is to obtain the one-dimensional illuminant invariant image of the microscopic image by using the method of Finlayson et al. [31]. This operation will convert the original RGB image into a grayscale version meanwhile removing the influence of illumination. The equation is defined as:

$$I^{inv}(r,c) = \exp(\pmb{\Gamma}_1(r,c)\cos(\theta) + \pmb{\Gamma}_2(r,c)\sin(\theta)) \quad (9)$$

where r and c are pixel position indexes of an image. θ is the projection direction in the two-dimensional log-chromaticity space of the microscopic image and it is a constant for a specific camera. This direction can be estimated by traversing every integer angle from 1° to 180° and it makes $\pmb{I}^{inv}$ having the minimum Shannon's entropy [31]. $\pmb{\Gamma}_1(r,c)$ and $\pmb{\Gamma}_2(r,c)$ is calculated by:

$$[\pmb{\Gamma}_1(r,c),\pmb{\Gamma}_2(r,c)]^T = [\pmb{v}_1,\pmb{v}_2]^T\pmb{\kappa}(r,c) \quad (10)$$

where $\pmb{v}_1 = \left[\frac{1}{\sqrt{2}}, -\frac{1}{\sqrt{2}}, 0\right]^T$, $\pmb{v}_1 = \left[\frac{1}{\sqrt{6}}, \frac{1}{\sqrt{6}}, -\frac{2}{\sqrt{6}}\right]^T$. $\pmb{\kappa}(r,c)$ is defined by:

$$\pmb{\kappa}(r,c) = \left[\ln\left(\frac{\pmb{R}(r,c)}{\pmb{\Lambda}(r,c)}\right), \ln\left(\frac{\pmb{G}(r,c)}{\pmb{\Lambda}(r,c)}\right), \ln\left(\frac{\pmb{B}(r,c)}{\pmb{\Lambda}(r,c)}\right)\right]^T \quad (11)$$

where $\pmb{\Lambda}(r,c) = \sqrt[3]{\pmb{R}(r,c)\pmb{G}(r,c)\pmb{B}(r,c)}$. $\pmb{R}(r,c)$, $\pmb{G}(r,c)$ and $\pmb{B}(r,c)$ are the three components of a color image.

In operation 2 (OPB2), the binary version of $\pmb{I}^{inv}$ can be generated by using the following simple thresholding segmentation method:

$$\pmb{I}^{bw}(r,c) = \begin{cases} 0, & \text{if } \pmb{I}^{inv}(r,c) < \tau \\ 1, & \text{if } \pmb{I}^{inv}(r,c) \geq \tau \end{cases} \quad (12)$$

where $\pmb{I}^{bw}$ denotes the binary image after thresholding and τ is selected based on empirical trials. Operation 3 (OPB3) uses the same two successive morphological operations as in OPA3 for the same purpose of refining object boundaries. Finally, in operation 4 (OPB4), the mask image is gained by down-sampling the result of OPB3 into the EIT image size. An example of the second segmentation algorithm is illustrated in Fig. 4.

2) Pixel Grouping: Based on the mask image, EIT image pixels in the same connected white region of the mask image will be considered to have a similar structure and are labelled as the same large group. The other individual pixels will be labelled as small groups. Examples of grouping results can be found in Table III. It should be noted that each large group contains more than one pixel, and each small group only contains one pixel. Suppose the pixels of the EIT image can be classified into N groups, the underlying conductivity change can be expressed as:

$$\Delta\pmb{\sigma} = \left\{\Delta\pmb{\sigma}_{g_1}, \Delta\pmb{\sigma}_{g_2}, \dots, \Delta\pmb{\sigma}_{g_N}\right\} \quad (13)$$

where $g_i, i = 1, 2, \dots, N$, represents group index of the ith group. This expression should satisfy the properties of $\Delta\pmb{\sigma} = \bigcup_{i=1}^N \Delta\pmb{\sigma}_{g_i}$ and $\Delta\pmb{\sigma}_{g_i} \bigcap \Delta\pmb{\sigma}_{g_j} = \emptyset$ for any $i \neq j$.

3) Optimization Solving: The key idea of IGGS is to incorporate structural information from the optical image by using group sparsity regularization. Group sparsity groups pixels with structural similarities and apply sparsity constraint on the formed pixel groups. Therefore, the grouping result from the second step of IGGS will guide the formulation of the group-level regularization term. The vanilla form of group sparsity can be expressed by the following $l_{2,1}$ norm [32]:
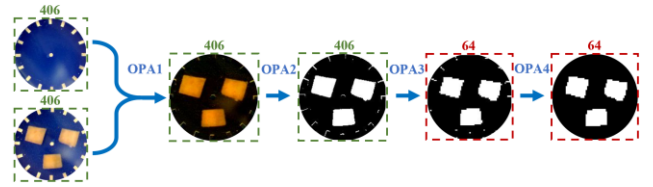

Fig. 3. An example of semantic segmentation for EIT sensor A based dual-modal sensor. The leftist images are carrot image (bottom) and calibration image (top), and the rightest image is the mask image. Numbers mean the pixel numbers of the side of the circumscribed square region.
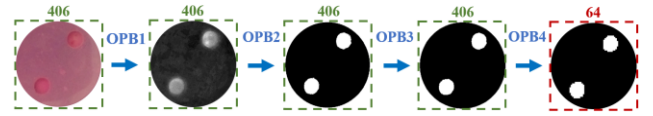

Fig. 4. An example of semantic segmentation for EIT sensor B based dual-modal sensor. The leftist image is the cell spheroid image and the rightest image is the mask image. Numbers mean the pixel numbers of the side of the circumscribed square region.

$$\|\Delta\pmb{\sigma}\|_{2,1} = \sum_{i=1}^N \|\Delta\pmb{\sigma}_{g_i}\|_2 \quad (14)$$

In this work, we adopt weighted group sparsity and the ultimate optimization problem for IGGS based on weighted group-level constraint and Total Variation (TV) constraint can be formulated by the below equations:

$$\begin{cases} \min_{\pmb{\sigma}} & \sum_{i=1}^N \omega_i\|\Delta\pmb{\sigma}_{g_i}\|_2 + \|\Delta\pmb{\sigma}\|_{TV} \\ \text{s.t.} & \pmb{J}\Delta\pmb{\sigma} = \Delta\pmb{V} \end{cases} \quad (15)$$

where $\sum_{i=1}^N \omega_i\|\Delta\pmb{\sigma}_{g_i}\|_2$ is the weighted $l_{2,1}$ norm and ω_i is the weight for ith group. $\|\Delta\pmb{\sigma}\|_{TV}$ is the isotropic *TV* norm, which can help smooth the estimated EIT image and is defined as [33]:

$$\|\Delta\pmb{\sigma}\|_{TV} = \sum_{r,c} \sqrt{(D_{r,c}^h(\Delta\pmb{\sigma}))^2 + (D_{r,c}^v(\Delta\pmb{\sigma}))^2} \quad (16)$$

where $D_{r,c}^h(\Delta\pmb{\sigma})$ and $D_{r,c}^v(\Delta\pmb{\sigma})$ is the first order finite difference operators in horizontal direction and vertical direction, respectively. And these two operators are defined by (17) and (18), respectively:

$$D_{r,c}^h(\Delta\pmb{\sigma}) = \begin{cases} \Delta\pmb{\sigma}_{r,c} - \Delta\pmb{\sigma}_{r,c+1}, & 1 \leq c \leq h_n \\ 0, & c = v_n \end{cases} \quad (17)$$

$$D_{r,c}^v(\Delta\pmb{\sigma}) = \begin{cases} \Delta\pmb{\sigma}_{r,c} - \Delta\pmb{\sigma}_{r+1,c}, & 1 \leq r \leq v_n \\ 0, & r = v_n \end{cases} \quad (18)$$

where h_n denotes the pixel number along the horizontal direction and v_n denotes the pixel number along the vertical direction.

To solve (15), the accelerated ADMM (A-ADMM) is used, which exhibits faster convergence than the conventional ADMM by including an over-relaxation step [26]. By introducing an auxiliary vector, $\pmb{a}$, (15) can be equivalently rewritten as:

$$\begin{cases} \min_{\Delta\sigma} \sum_{i=1}^{N} \omega_i \|a_{g_i}\|_2 + \|\Delta\sigma\|_{TV} & (19) \\ \text{s.t.} \quad a = \Delta\sigma, \ J\Delta\sigma = \Delta V n \end{cases}$$

Equation (19) can be solved by the augmented Lagrangian scheme and its equivalent augmented Lagrangian problem is formulated as:

$$\min_{\Delta\sigma,a} \left\{ \sum_{i=1}^{N} \omega_i \|a_{g_i}\|_2 + \|\Delta\sigma\|_{TV} - \lambda_1^T(a - \Delta\sigma) \right.$$
$$+ \frac{\eta_1}{2} \|a - \Delta\sigma\|_2^2 - \lambda_2^T(J\Delta\sigma - \Delta V)$$
$$\left. + \frac{\eta_2}{2} \|J\Delta\sigma - \Delta V\|_2^2 \right\} \qquad (20)$$

where λ_1 and λ_2 represents multipliers; η_1 and η_2 are penalty parameters. In the A-ADMM framework, (20) is decomposed into following $\Delta\sigma$-subproblem (21) and a-subproblem (22), and these two subproblems can be solved separately.

$$\Delta\sigma^{k+1} = \arg\min_{\Delta\sigma} \left\{ \|\Delta\sigma^k\|_{TV} + \lambda_1^T\Delta\sigma^k + \frac{\eta_1}{2} \|a - \Delta\sigma^k\|_2^2 \right.$$
$$\left. -\lambda_2^T J\Delta\sigma^k + \frac{\eta_2}{2} \|J\Delta\sigma^k - \Delta V\|_2^2 \right\} \qquad (21)$$

$$a^{k+1} = \arg\min_{a} \left\{ \sum_{i=1}^{N} \omega_i \|a_{g_i}^k\|_2 - \lambda_1^T a^k + \frac{\eta_1}{2} \|a - \Delta\sigma^k\|_2^2 \right\}$$
$$(22)$$

The $\Delta\sigma$-subproblem (21) is solved by a gradient-based recovery algorithm, and each iteration equation is expressed as:

$$\Delta\sigma^{k+1} = \Delta\sigma^k - \mu\{J^T(\eta_2 J\Delta\sigma^k - \eta_2\Delta V - \lambda_2) + \lambda_1$$
$$+ \eta_1(\Delta\sigma^k - a) + \nabla\|\Delta\sigma^k\|_{TV}\} \quad (23)$$

where μ is the iteration step length, and the gradient of TV norm based on a smooth approximation strategy is calculated by:

$$\nabla_{r,c}\|\Delta\sigma\|_{TV} = \frac{D_{r,c}^h(\Delta\sigma) + D_{r,c}^v(\Delta\sigma)}{\sqrt{(D_{r,c}^h(\Delta\sigma))^2 + (D_{r,c}^v(\Delta\sigma))^2 + \varphi}}$$
$$- \frac{D_{r,c-1}^h(\Delta\sigma)}{\sqrt{(D_{r,c-1}^h(\Delta\sigma))^2 + (D_{r,c-1}^v(\Delta\sigma))^2 + \varphi}}$$
$$- \frac{D_{r-1,c}^v(\Delta\sigma)}{\sqrt{(D_{r-1,c}^h(\Delta\sigma))^2 + (D_{r-1,c}^v(\Delta\sigma))^2 + \varphi}}$$
$$(24)$$

where φ is the relaxation factor, which can avoid the occurrence of zero denominator in the gradient of TV norm and should not be too large. φ is set as 1×10^{-7} throughout this paper based on a series of trials.

The a-subproblem (22) is solved by the below group-wise soft thresholding [34]:

$$a_{g_i} = \max\left\{\left\|\Delta\sigma_{g_i} + \frac{1}{\eta_1}(\lambda_1)_{g_i}\right\|_2 - \frac{\omega_i}{\eta_1}, 0\right\} \frac{\Delta\sigma_{g_i} + \frac{1}{\eta_1}(\lambda_1)_{g_i}}{\left\|\Delta\sigma_{g_i} + \frac{1}{\eta_1}(\lambda_1)_{g_i}\right\|_2}$$
$$(25)$$

After solving the $\Delta\sigma$-subproblem and a-subproblem successively, an additional constraint is posed on the solution of the a-subproblem followed by the updates of multipliers based on the accelerated method. The additional constraint can improve the algorithm's ability of voltage noise resistance and is defined as:

$$AP_{i=1}^{N}\left(\text{sign}_{gi}(\text{sum}_{gi}(a))\right) \cdot a \geq 0 \qquad (26)$$

where $\text{sum}_{g_i}()$ denotes the summation of all elements of a_{g_i}. $\text{sign}_{g_i}()$ means the operation of assigning the value of the $\text{sign}(\text{sum}_{g_i}(a))$ to each pixel of ith group; here, $\text{sign}()$ is the sign function. $AP_{i=1}^{N}()$ mean applying $\text{sign}_{g_i}(\text{sum}_{g_i}(a))$ to all groups. This constraint imposes non-negative constraint to the groups with the number one resulting from $\text{sign}_{g_i}(\text{sum}_{g_i}(a))$ and imposes non-positive constraint to the groups with the number minus one resulting from the same equation. By this approach, it is expected that the artefact around the imaging targets can be effectively eliminated. Then, the update of multipliers based on the accelerated method is carried out according to the following equations:

$$\begin{cases} \tilde{\lambda}_1^{k+1} = \lambda_1^k - \varepsilon_1\eta_1(a^{k+1} - \Delta\sigma^{k+1}) \\ \tilde{\lambda}_2^{k+1} = \lambda_2^k - \varepsilon_2\eta_2(J\Delta\sigma^{k+1} - \Delta V) \\ d^{k+1} = \frac{1 + \sqrt{1 + 4(d^k)^2}}{2} \\ a^{k+1} = a^{k+1} + \frac{d^k - 1}{d^{k+1}}(a^{k+1} - a^k) \\ \lambda_1^{k+1} = \tilde{\lambda}_1^{k+1} + \frac{d^k - 1}{d^{k+1}}(\tilde{\lambda}_1^{k+1} - \tilde{\lambda}_1^k) \\ \lambda_2^{k+1} = \tilde{\lambda}_2^{k+1} + \frac{d^k - 1}{d^{k+1}}(\tilde{\lambda}_2^{k+1} - \tilde{\lambda}_2^k) \end{cases} \qquad (27)$$

where, ε_1 and ε_2 are the iteration step lengths. d is an additional variable for the predictor-corrector–type acceleration process and its initial value is set as 1 throughout the paper.

IGGS adopts two stopping criteria in solving (15), i.e. the maximum iteration number and following condition:

$$\|\Delta\sigma^{k+1} - \Delta\sigma^k\|_2 < \wp \qquad (28)$$

$\wp$ is the tolerance. The IGGS will stop if either of the two criteria is satisfied. In addition, throughout the paper, weights selection is based on the following equation, which can promote the sparsity for large group conductivity estimation [17].

$$\omega_i = \begin{cases} \dfrac{1}{2N_s + N_l} & \text{if } i^{\text{th}} \text{ group is large} \\ \dfrac{2}{2N_s + N_l} & \text{if } i^{\text{th}} \text{ group is small} \end{cases} \qquad (29)$$

Algorithm: Image-Guided Group Sparsity (IGGS)
Input: Jacobian matrix J, voltage change measurements ΔV and weight vector ω, η_1, η_2, ε_1, ε_2.
Initialize: $\Delta\sigma$ equals to the result of Tikhonov regularization. $a = \Delta\sigma$, $\lambda_1 = 0$, $\lambda_2 = 0$, $d = 1$.
Step 1: Semantic segmentation for guidance image by application-specific algorithm.
Step 2: Pixel grouping according to the method depicted in section III-B-2).
Step 3: Iteration until satisfying stopping criteria, Do: ① Solve subproblem (20) by using (22). ② Solve subproblem (21) by using (24). ③ Apply constraint (25) to the result of ②. ④ Update multipliers by using (26). End Do.
Output: The estimated conductivity change distribution.
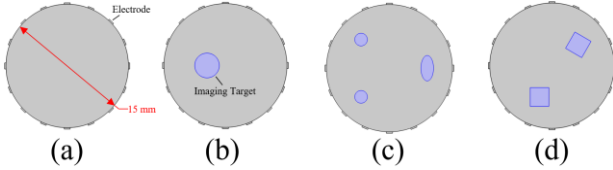
Fig. 5. Modelled (a) 16-electrode EIT sensor, (b) phantom 1, (c) phantom 2 and (d) phantom 3.

where N_s and N_l are the number of small groups and the number of large groups, respectively. They also satisfy $N_s + N_l = N$, N is the number of total groups.

To sum up, the implementation of the whole IGGS algorithm is illustrated in Table I.

IV. RESULTS AND DISCUSSION

The proposed IGGS algorithm is evaluated by numerical simulation and real-world experiments. The performance of IGGS is compared with that of other widely used single-modal based EIT image reconstruction algorithms, i.e. the classical Tikhonov regularization based algorithm (TReg) [27] and the state-of-the-art Structure-Aware Sparse Bayesian Learning (SA-SBL) [19] and Enhanced Adaptive Group Sparsity with Total Variation (EAGS-TV) [18] algorithms. The numerical simulation aims to quantitatively evaluate the performance of the algorithms and real-world experiments are to verify the practical feasibility.

A. Numerical Simulation

1) Modelling: A 16-electrode EIT sensor is modelled in COMSOL Multiphysics (see Fig. 5 (a)). The diameter of the sensor is 15 mm and the background medium is set as homogeneous saline with a conductivity value of 0.05 S/m^{-1}. The material of electrodes is set as Titanium whose conductivity is 7.407×10^5 S/m^{-1}. From Fig. 5 (b) to Fig. 5 (d), three types of conductivity distribution, i.e. phantom 1 to

phantom 3, are modeled. The background material of all phantoms is saline with the conductivity value of 0.05 S/m^{-1}. Phantom 1 simulates a large circle object with a conductivity value of 0.035 S/m^{-1}. Phantom 2 simulates three dispersed small objects. i.e. two circle with conductivity values of 0.035 S/m^{-1} (upper left) and 0.015 S/m^{-1} (bottom left) respectively, and a ellipse object with conductivity value of 0.025 S/m^{-1}. Phantom 3 simulates two square objects with conductivity values of 0.08 S/m^{-1} (upper right) and 0.035 S/m^{-1} (bottom) respectively. The adjacent sensing protocol is applied to obtain the boundary voltage data [35].

2) Parameter Settings: The regularization factor of TReg is searched based on the L-curve method [36]. The calculated optimal regularization factors for phantom 1, phantom 2 and phantom 3 are 9.2140×10^{-11}, 2.5655×10^{-6} and 1.1153×10^{-6}, respectively. Parameters of other algorithms are determined based on trial and error to ensure the best performance of the algorithms within a wide range of parameter sets. For all results based on SA-SBL, the maximum iteration number is set as 5 and the tolerance is selected as 1×10^{-5}; the pattern coupling factor and the cluster size are chosen as 0.3 and 4, respectively. For EAGS-TV and IGGS, the result of Treg with the regularization factor of 0.001 is selected as their starting point and the weight calculation is based on (29). The maximum iteration number of IGGS is set as 90 for phantom 1 and phantom 2 and set as 40 for phantom 3. The stopping tolerance of IGGS for all phantoms is set as 1×10^{-7}. The iteration number and stopping tolerance are set as 150 and 1×10^{-7} for all cases based on EAGS-TV. For IGGS, the penalty parameters η_1 and η_2 are set as $0.0015/\text{mean}(\text{abs}(\Delta V))$ and $0.0005/\text{mean}(\text{abs}(\Delta V))$. abs() converts each element of ΔV to its absolute value and the function of mean() is to calculate the average value of the vector abs(ΔV). The multiplier update step lengths ε_1 and ε_2 are both selected as 0.4854. The two multiplier update step lengths for EAGS-TV are same and are set as 0.9870. In EAGS-TV, the penalty parameter for the l_2 norm related to auxiliary variable is set as $1/\text{mean}(\text{abs}(\Delta V))$ and the penalty parameter for the l_2 norm related to EIT linearized model is set as $10/\text{mean}(\text{abs}(V))$. In addition, the maximum group diameter for EAGS-TV is set as 10 pixels, which is reasonable in this study. If not specified, algorithm parameter settings follow the above configuration in the following discussions.

3) Quantitative Metrics: In simulation, as the ground truth is known, the reconstructed image can be quantitatively evaluated by two metrics, i.e. Relative Image Error (RIE) and Mean Structural Similarity Index (MSSIM) [37], which are defined as:
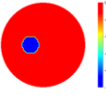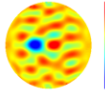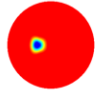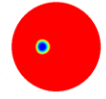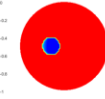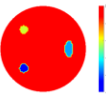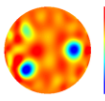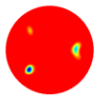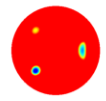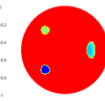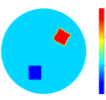
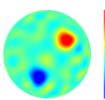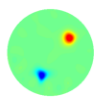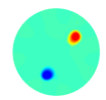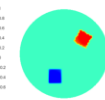$$\text{RIE} = \frac{\|E - G\|_2}{\|G\|_2} \tag{30}$$

$$\text{MSSIM} = \frac{1}{WH}\sum_r\sum_c \frac{(2\mu_E\mu_G + C_1)(2\delta_{EG} + C_2)}{(\mu_E^2 + \mu_G^2 + C_1)(\delta_E^2 + \delta_G^2 + C_2)} \tag{31}$$

where E and G are the reconstructed image and the ground truth, respectively. W and H are the width and height of an image.
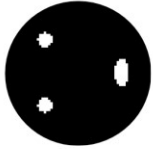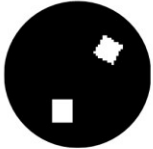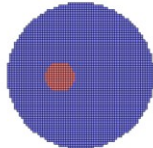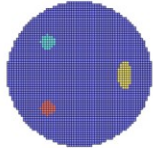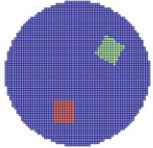
$\mu_E = \mu_E(r,c)$, $\mu_G = \mu_G(r,c)$, $\delta_E = \delta_E(r,c)$, $\delta_G = \delta_G(r,c)$, and $\delta_{EG} = \delta_{EG}(r,c)$ are the local means, standard deviations and cross-covariance for E and G. $C_1 = (K_1L)^2$ and $C_2 = (K_2L)^2$. K_1 and K_2 are constants with values of 0.01 and 0.03, respectively. As the absolute pixel values of the reconstructed EIT images in both simulation study and real-world experiments are normalized to [0, 1] in this work, L is set as 1.

4) Result Comparison and Discussion: Table II displays the reconstructed EIT images, RIE and MSSIM based on IGGS, TReg, SA-SBL and EAGS-TV. In these results, the voltage data is noise-free and the mask image for IGGS is accurate and generated by assigning one to pixels where there are objects and assigning zero to the background pixels. The mask images and corresponding grouping results are shown in Table III. In Table III, LNG means the number of large groups and SNG means the number of small groups. When a mask image is given, the grouping results can be easily acquired by the method in Section III-B-2). Thus, for later reconstructed images by IGGS, we only provide mask images. According to Table II, although TReg can predict the position of objects correctly, the shape and conductivity contrasts are significantly wrong (see its images, RIE and MSSIM) and this algorithm suffers from severe background noise. SA-SBL and AGS-TV show considerable improvement in terms of the accuracy of the shape and conductivity contrasts. When the shape of the imaging objects are circle and ellipse, they can predict a relatively accurate shape. However, these two algorithms are powerless when encountering imaging objects with angles and straight lines like phantom 3 and the shape feature is lost. Differently, IGGS can generate the most accurate position, shape, and conductivity contrasts.

Table IV selects phantom 2 to compare noise resistance ability of algorithms with signal to noise ratios (SNR) of 35 dB and 25 dB. Since the voltage data are changed, the regularization factors of TReg for phantom 2 should be re-calculated based on the L-curve method [36]. The searched regularization factors for voltage data with the SNR of 35 dB and 25 dB are 3.5384×10^{-6} and 1.7933×10^{-5},

respectively. As shown in the Table II and Table IV, EAGS-TV presents a good noise-resistance ability. The shape of objects in the reconstructed images of this algorithm does not change significantly and the RIE varies within 0.03. The performance of SA-SBL is a worse than EAGS-TV, which can be indicated by the reconstructed shape and quantitative metrics. However, images generated by these two algorithms show evident change when SNR varies from 35 dB to 25 dB. In this case, the images generated by TReg show unnoticeable degradation. Meanwhile, the results of IGGS also show slight change when SNR decreases. The performance of IGGS presents the highest level compared with other algorithms, which indicates IGGS has the best noise resistance capability among these four given algorithms.

Table V selects phantom 3 to examine the noise-resistance ability of IGGS under noise-contaminated voltage data and inaccurate mask image. Two voltage noise-levels, i.e. clean voltage data an d voltage data with SNR=35 dB, are selected. In addition, the mask image suffers from three perturbation-levels, i.e. accurate mask, slight perturbed mask and severely perturbed mask (from top to bottom). Inaccurate mask may be generated by the unideal semantic segmentation algorithms or caused by noisy guidance image in real scenarios. Therefore, investigation of the effect of inaccurate mask image is necessary for real applications. As Table V shows, the shape of objects in the reconstructed image is determined by the mask image. Given a fixed mask image, quantitative metrics are barely influenced by the voltage noise. While given a fixed voltage noise-level, the metrics become worse when the mask image becomes inaccurate. However, the quantitative metrics of the results of IGGS is still superior to those images generated by the other three algorithms under the same voltage noise-level. In addition, although given an inaccurate mask, the conductivity change can still be estimated relatively accurate except the pixels at the boundary. This indicates IGGS has a good generalization ability when encountering inaccurate mask images. In summary, IGGS has a strong ability to resist voltage noise and mask perturbation.

TABLE IV
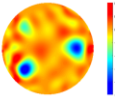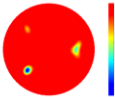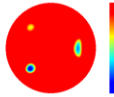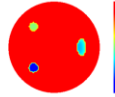COMPARISON OF THE ABILITY OF VOLTAGE NOISE RESISTANCE
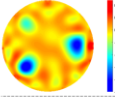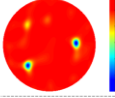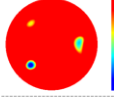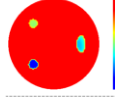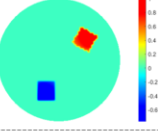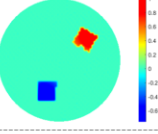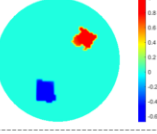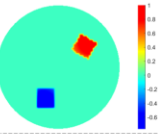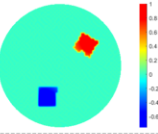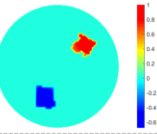
Noise Level	TReg	SA-SBL	EAGS-TV	IGGS
SNR=35 dB				
RIE MSSIM	0.9532 0.2805	0.6279 0.7970	0.4501 0.8910	0.1333 0.9661
SNR=25 dB				
RIE MSSIM	1.0253 0.2545	0.6519 0.6356	0.4752 0.8860	0.1323 0.9627

TABLE V
IMAGE RECONSTRUCTION RESULTS BASED ON INACCURATE MASK
IMAGE

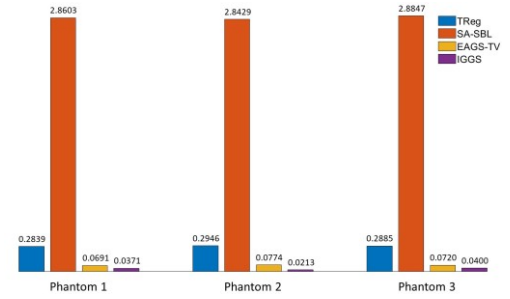| Mask Image			
Clean Voltage			
RIE MSSIM	0.2445 0.9732	0.2906 0.9662	0.3642 0.9529
SNR=35 dB			
RIE MSSIM	0.2450 0.9732	0.2897 0.9663	0.3650 0.9527

Fig. 6. Running time comparison. The values represent the running time (unit: second).
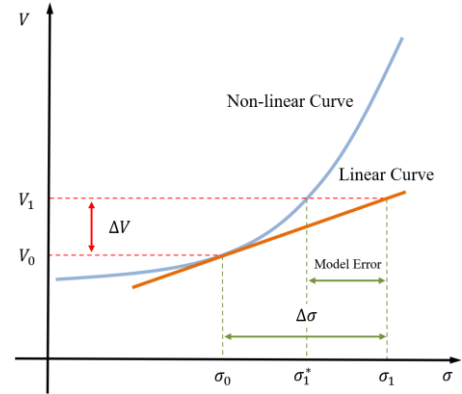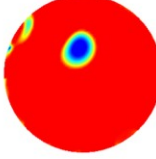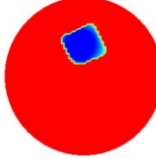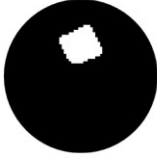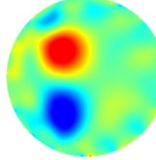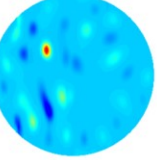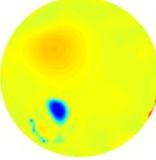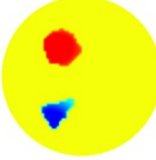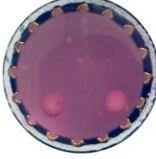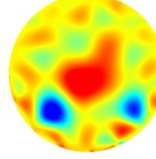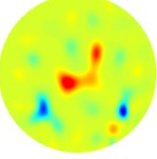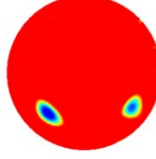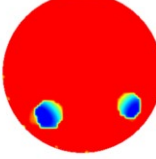
Fig. 7. Induced boundary voltage response of EIT. Linearization leads to the model error.
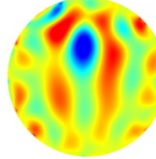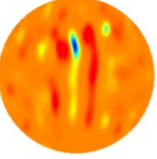
The last comparison is concerned with the elapsed time. As the second and third steps of IGGS are fixed in practice and we don't conduct semantic segmentation in sumulation, we only compare the elapsed time of the second and third steps of IGGS with the other algorithms. The simulation data and algorithm parameter settings are the same as those in Table II. The results are illustrated in Fig. 6. The image reconstruction is carried out on the MATLAB R2021a on a Windows laptop with an Intel[R] Core[TM] i7-10750 CPU. From Fig. 6, it is explicit that IGGS spends the minimum time for all phantoms, while TReg and SA-SBL are the two most time-consuming algorithms. Comparing IGGS with EAGS-TV, the less elapsed time is mainly benefited from smaller number of iterations, indicating IGGS has the potential to be implemented for real-time image reconstruction in future applications.

Here we also present a brief discussion of the model error and its influences. In the adopted time-difference imaging model, the model error originates from the linearization of the non-linear problem of EIT. Specificlly, the forward model of EIT, i.e. (1), is a non-linear mapping, while this paper adopts the commonly used linearized version, i.e. (2). Based on the linearized forward model, the EIT image reconstruction cannot recover accurate conductivity change distribution when the perturbation is not subtle. This is the primary reason that we normalize the reconstructed images and focus on the contrasts of the conductivity distribution. We qualitatively discuss the model error with the assistance of Fig. 7. In Fig. 7, we ignore all types of measurement error and confine F as a mapping from $\mathbb{R}$ to $\mathbb{R}$. Thus, the vector $\boldsymbol{\sigma}$ and $\boldsymbol{V}$ are simplified as the scalar σ and scalar V, respectively. The blue curve represents the true EIT forward response and the orange straight line represents the linearized forward response. Note this simplification and the curves are just for illustration purpose. At the reference time point, the conductivity is denoted by σ_0 and the corresponding boundary voltage is represented by V_0. V_1 denotes the boundary voltage at the observation time point. Based on the linear model and the voltage measurement $\Delta V = V_1 - V_0$, the reconstructed conductivity change is $\Delta \sigma = \sigma_1 - \sigma_0$. However, it should be $\sigma_1^* - \sigma_0$ according to the realistic non-linear model. Such deviation would affect the image reconstruction quality and accuracy in practical applications.

B. Real-world Experiments

The performance of IGGS is further validated on real-world data and the results are illustrated in Table VI. The sensor is

TABLE VI
IMAGE RECONSTRUCTION COMPARISON BASED ON EXPERIMENTAL DATA

Phantom	TReg	SA-SBL	EAGS-TV	IGGS
MSSIM	0.1767	0.5334	0.7836	0.8147
MSSIM	0.2073	0.5035	0.5190	0.8872
MSSIM	0.2536	0.4750	0.6899	0.8199

connected to the EIT system developed in the Intelligent Sensing, Analysis and Control Group (ISAC) at The University of Edinburgh and the highest Signal-to-Noise Ratio (SNR) of the system is 82.82 dB [38]. As stated in Section III, we use two EIT sensors, i.e. EIT sensor A and EIT sensor B, to verify the proposed method. EIT sensor A is used to image square carrot tissues (length ~ 3 mm) and the combination of a triangle rubber (large length ~ 3 mm, small length ~ 2mm) and a hexagonal iron (diameter ~ 3 mm). The Background medium for both phantoms is saline, which conductivity is 0.05 S/m^{-1}. The upper surface of the iron is covered by a thin white rubber layer. The rubber layer does not affect the conductivity properties of this imaging target much, meanwhile, it can reduce surface reflection that may influence the definition of the object shape in the optical image. The EIT sensor B is employed to image MCF-7 cell spheroids (diameter ~ 2 mm) which are cultured in PBS with a conductivity of 2 S/m^{-1}. For all experiments, the current excitation frequency is set as 10 kHz and the current amplitude is set as 1.5 mA peak to peak. A completed frame contains 104 individual measurements, and the frame rate is 48 fps. Adjacent protocol is also adopted to collect boundary voltages [35].

Based on the L-curve method [36], the searched Tikhonov regularization factors for carrot tissues, the combination of a triangle rubber and a hexagonal iron, and MCF-7 cell spheroids are 2.5109×10^{-5}, 0.0015 and 2.4612×10^{-5}, respectively. In addition, based on trials, the maximum iteration numbers are set as 100 and 40 for EAGS-TV and IGGS, for all experiments. In rubber and iron imaging, the penalty parameter for the l_2 norm related to auxiliary variable is set as 0.05/mean(abs(ΔV))

and the penalty parameter for the l_2 norm related to EIT linearized model is set as 10/mean(abs(ΔV)) for EAGS-TV. Other parameters for all algorithms and all experiments are set the same as those in simulation study. In addition, the size of structuring element is set as 3×3 for the two sets of segmentation algorithms throughout experiments. For the cell spheroid image segmentation, the value of τ is set as 0.45.

In Table VI, mask images generated by the semantic segmentation algorithms are in the rightest column. We assume the mask images provide accurate geometrical distribution information and select them as the reference to calculate MSSIM for quantitative assessment of algorithm performance. For TReg and SA-SBL, the shape of imaging targets is deteriorated, and the images contain too much background noise although they can roughly locate the position of imaging targets. EAGS-TV has a stronger capability of noise resistance compared to the former two methods, whereas it fails to reconstruct objects with accurate shapes. In contrast, only IGGS presents the best shape preservation ability (see images and MSSIM) and background noise-resistance ability (see image background quality) for different types of miniature sensors and sensing objects.

V. CONCLUSION

We proposed an EIT-optical dual-modal image reconstruction algorithm named IGGS to improve the image quality of EIT with the assistance of an extra imaging modality. IGGS fuses the dual-modal information from EIT and optical images to reconstruct high-quality EIT images. Both simulation study and real-world experiments demonstrated that IGGS

could generate more accurate contrasts of conductivity distribution than the comparative algorithms, implying the potential of performing impedance-based quantitative analysis for tissue engineering. Future research will extend the method to the three-dimensional imaging setup. Quantitative conductivity imaging based on the dual-modal setup will also be rigorously explored.

References

[1] R. H. Bayford, "Bioimpedance tomography (electrical impedance tomography)," *Annu. Rev. Biomed. Eng.,* vol. 8, pp. 63-91, 2006.

[2] P. Metherall, D. C. Barber, R. H. Smallwood, and B. H. Brown, "Three-dimensional electrical impedance tomography," *Nature,* vol. 380, no. 6574, pp. 509-512, 1996.

[3] D. S. Holder, *Electrical impedance tomography: methods, history and applications*. CRC Press, 2004.

[4] A. Seppänen, A. Voutilainen, and J. Kaipio, "State estimation in process tomography—reconstruction of velocity fields using EIT," *Inverse Problems,* vol. 25, no. 8, p. 085009, 2009.

[5] H. S. Tapp, A. Peyton, E. K. Kemsley, and R. H. Wilson, "Chemical engineering applications of electrical process tomography," *Sensors and Actuators B: Chemical,* vol. 92, no. 1-2, pp. 17-24, 2003.

[6] C. Dang, M. Darnajou, C. Bellis, G. Ricciardi, S. Mylvaganam, and S. Boure nnane, "Improving EIT-based visualizations of two-phase flows using an eigenvalue correlation method," *IEEE Transactions on Instrumentation and Measurement,* vol. 70, pp. 1-9, 2021.

[7] D. Santos, P. Faia, F. Garcia, and M. Rasteiro, "Oil/water stratified flow in a horizontal pipe: Simulated and experimental studies using EIT," *Journal of Petroleum Science and Engineering,* vol. 174, pp. 1179-1193, 2019.

[8] Y. Yang, J. Jia, S. Smith, N. Jamil, W. Gamal, and P.-O. Bagnaninchi, "A miniature electrical impedance tomography sensor and 3-D image reconstruction for cell imaging," *IEEE Sensors Journal,* vol. 17, no. 2, pp. 514-523, 2016.

[9] Y. Yang, H. Wu, J. Jia, and P.-O. Bagnaninchi, "Scaffold-based 3-D cell culture imaging using a miniature electrical impedance tomography sensor," *IEEE Sensors Journal,* vol. 19, no. 20, pp. 9071-9080, 2019.

[10] H. Wu, Y. Yang, P. O. Bagnaninchi, and J. Jia, "Electrical impedance tomography for real-time and label-free cellular viability assays of 3D tumour spheroids," *Analyst,* vol. 143, no. 17, pp. 4189-4198, 2018.

[11] B. Gong, B . Schullcke, S. Krueger-Ziolek, F. Zhang, U. Mueller-Lisse, and K. Moeller , "Higher order total variation regularization for EIT reconstruction," *Medical & biological engineering & computing,* vol. 56, no. 8, pp. 1367-1378, 2018.

[12] J. Liu, L. Lin, W. Zhang, and G. Li, "A novel combined regularization algorithm of total variation and Tikhonov regularization for open electrical impedance tomography," *Physiological measurement,* vol. 34, no. 7, p. 823, 2013.

[13] K. Lee, E. J. Woo, and J. K. Seo, "A fidelity-embedded regularization method for robust electrical impedance tomography," *IEEE transactions on medical imaging,* vol. 37, no. 9, pp. 1970-1977, 2017.

[14] J. Li, S. Yue, M. Ding, Z. Cui, and H. Wang, "Adaptive Lp Regularization for Electrical Impedance Tomography," *IEEE Sensors Journal,* vol. 19, no. 24, pp. 12297-12305, 2019.

[15] M. Gehre *et al.*, "Sparsity reconstruction in electrical impedance tomography: an experimental evaluation," *Journal of Computational and Applied Mathematics,* vol. 236, no. 8, pp. 2126-2136, 2012.

[16] Y. Shi, Y. Wu, M. Wang, Z. Tian, X. Kong, and X. He, "Sparse image reconstruction of intracerebral hemorrhage with electrical impedance tomography," *Journal of Medical Imaging,* vol. 8, no. 1, p. 014501, 2021.

[17] Y. Yang and J. Jia, "An image reconstruction algorithm for electrical impedance tomography using adaptive group sparsity constraint," *IEEE Transactions on Instrumentation and Measurement,* vol. 66, no. 9, pp. 2295-2305, 2017.

[18] Y. Yang, H. Wu, and J. Jia, "Image reconstruction for electrical impedance tomography using enhanced adaptive group sparsity with total variation," *IEEE Sensors Journal,* vol. 17, no. 17, pp. 5589-5598, 2017.

[19] S. Liu, J. Jia, Y. D. Zhang, and Y. Yang, "Image reconstruction in electrical impedance tomography based on structure-aware sparse Bayesian learning," *IEEE transactions on medical imaging,* vol. 37, no. 9, pp. 2090-2102, 2018.

[20] D. Liu, D. Gu, D. Smyl, A. K. Khambampati, J. Deng, and J. Du, "Shape-driven EIT reconstruction using Fourier representations," *IEEE Transactions on Medical Imaging,* 2020.

[21] D. Liu, D. Gu, D. Smyl, J. Deng, and J. Du, "Shape reconstruction using Boolean operations in electrical impedance tomography," *IEEE transactions on medical imaging,* vol. 39, no. 9, pp. 2954-2964, 2020.

[22] D. Liu, D. Gu, D. Smyl, J. Deng, and J. Du, "B-spline-based sharp feature preserving shape reconstruction approach for electrical impedance tomography," *IEEE transactions on medical imaging,* vol. 38, no. 11, pp. 2533-2544, 2019.

[23] Z. Li, J. Zhang, D. Liu, and J. Du, "CT image-guided electrical impedance tomography for medical imaging," *IEEE transactions on medical imaging,* vol. 39, no. 6, pp. 1822-1832, 2019.

[24] H. Liu, S. Zhao, C. Tan, and F. Dong, "A bilateral constrained image reconstruction method using electrical impedance tomography and ultrasonic measurement," *IEEE Sensors Journal,* vol. 19, no. 21, pp. 9883-9895, 2019.

[25] G. Liang, S. Ren, S. Zhao, and F. Dong, "A Lagrange-Newton method for EIT/UT dual-modality image reconstruction," *Sensors,* vol. 19, no. 9, p. 1966, 2019.

[26] T. Goldstein, B. O'Donoghue, S. Setzer, and R. Baraniuk, "Fast alternating direction optimization methods," *SIA M Journal on Imaging Sciences,* vol. 7, no. 3, pp. 1588-1623, 2014.

[27] M. Vauhkonen, D. Vadasz, P. A. Karjalainen, E. Somersalo, and J. P. Kaipio, "Tikhonov regularization and prior information in electrical impedance tomography," *IEEE transactions on medical imaging,* vol. 17, no. 2, pp. 285-293, 1998.

[28] W. R. Lionheart, "EIT reconstruction algorithms: pitfalls, challenges and recent developments," *Physiological measurement,* vol. 25, no. 1, p. 125, 2004.

[29] N. Otsu, "A threshold selection method from gray-level histograms," *IEEE transactions on systems, man, and cybernetics,* vol. 9, no. 1, pp. 62-66, 1979.

[30] R. C. Gonzalez and P. Wintz, "Digital image processing(Book)," *Reading, Mass., Addison-Wesley Publishing Co., Inc.(Applied Mathematics and Computation,* no. 13, p. 451, 1977.

[31] G. D. Finlayson, M. S. Drew, and C. Lu, "Entropy minimization for shadow removal," *International Journal of Computer Vision,* vol. 85, no. 1, pp. 35-57, 2009.

[32] J. Huang and T. Zhang, "The benefit of group sparsity," *The Annals of Statistics,* vol. 38, no. 4, pp. 1978-2004, 2010.

[33] A. Chambolle, "An a lgorithm for total variation minimization and applications," *Journal of Mathematical imaging and vision,* vol. 20, no. 1, pp. 89-97, 2004.

[34] W. Deng, W. Yin, and Y. Zhang, "Group sparse optimization by alternating direction method," in *Wavelets and Sparsity XV*, 2013, vol. 8858: International Society for Optics and Photonics, p. 88580R.

[35] B. H. Brown and A. D. Seagar, "The Sheffield data collection system," *Clinical Physics and Physiological Measurement,* vol. 8, no. 4A, p. 91, 1987.

[36] P. C. Hansen and D. P. O'Leary, "The use of the L-curve in the regularization of discrete ill-posed problems," *SIAM journal on scientific computing,* vol. 14, no. 6, pp. 1487-1503, 1993.

[37] Z. Wang, A. C. Bovik, H. R. Sheikh, and E. P. Simoncelli, "Image quality assessment: from error visibility to structural similarity," *IEEE transactions on image processing,* vol. 13, no. 4, pp. 600-612, 2004.

[38] Y. Yang and J. Jia, "A multi-frequency electrical impedance tomography system for real-time 2D and 3D imaging," *Revie w of Scientific Instruments,* vol. 88, no. 8, p. 085110, 2017.